nature geoscience

ARTICLES

https://doi.org/10.1038/s41561-018-0198-1

Rapid transition from continental breakup to igneous oceanic crust in the South China Sea

H. C. Larsen[1,2*], G. Mohn[3*], M. Nirrengarten[3], Z. Sun[4], J. Stock[5], Z. Jian[1], A. Klaus[6], C. A. Alvarez-Zarikian[6], J. Boaga[7], S. A. Bowden[8], A. Briais[9], Y. Chen[10], D. Cukur[11], K. Dadd[12], W. Ding[13], M. Dorais[14], E. C. Ferré[15], F. Ferreira[16], A. Furusawa[17], A. Gewecke[18], J. Hinojosa[5], T. W. Höfig[6], K. H. Hsiung[19], B. Huang[20], E. Huang[1], X. L. Huang[21], S. Jiang[22], H. Jin[1], B. G. Johnson[23], R. M. Kurzawski[24,25], C. Lei[26], B. Li[27], L. Li[1], Y. Li[28], J. Lin[4,29], C. Liu[30], C. Liu[1], Z. Liu[1], A. J. Luna[31], C. Lupi[32], A. McCarthy[33,50], L. Ningthoujam[34], N. Osono[35], D. W. Peate[36], P. Persaud[30], N. Qiu[4], C. Robinson[37], S. Satolli[38], I. Sauermilch[39], J. C. Schindlbeck[40], S. Skinner[41], S. Straub[42], X. Su[4], C. Su[43], L. Tian[44], F. M. van der Zwan[24,25], S. Wan[45], H. Wu[46], R. Xiang[4], R. Yadav[34], L. Yi[1], P. S. Yu[47], C. Zhang[4], J. Zhang[4], Y. Zhang[48], N. Zhao[29], G. Zhong[1] and L. Zhong[49]

Continental breakup represents the successful process of rifting and thinning of the continental lithosphere, leading to plate rupture and initiation of oceanic crust formation. Magmatism during breakup seems to follow a path of either excessive, transient magmatism (magma-rich margins) or of igneous starvation (magma-poor margins). The latter type is characterized by extreme continental lithospheric extension and mantle exhumation prior to igneous oceanic crust formation. Discovery of magma-poor margins has raised fundamental questions about the onset of ocean-floor type magmatism, and has guided interpretation of seismic data across many rifted margins, including the highly extended northern South China Sea margin. Here we report International Ocean Discovery Program drilling data from the northern South China Sea margin, testing the magma-poor margin model outside the North Atlantic. Contrary to expectations, results show initiation of Mid-Ocean Ridge basalt type magmatism during breakup, with a narrow and rapid transition into igneous oceanic crust. Coring and seismic data suggest that fast lithospheric extension without mantle exhumation generated a margin structure between the two endmembers. Asthenospheric upwelling yielding Mid-Ocean Ridge basalt-type magmatism from normal-temperature mantle during final breakup is interpreted to reflect rapid rifting within thin pre-rift lithosphere.

International Ocean Discovery Program (IODP) expeditions 367/368 at the northern South China Sea (SCS) margin (Fig. 1) addressed the spectrum of breakup processes defined by the two endmembers identified by North Atlantic drilling[1]: magma-rich and magma-poor margins[2,3]. The SCS margin, however, shows none of the expected characteristics of magma-rich margins[4,5], such as transient formation of excessively thick igneous crust (15–30 km) and more than 5-km-thick seaward-dipping reflectors (for example, the East Greenland margin[6,7]). Instead, its structural architecture, as inferred from seismic data, is reminiscent of a hyperextended 'magma-poor margin'[8–11]. Our findings provide the first well-constrained example of the 'missing link' between magma-rich margins and magma-poor, hyperextended margins. Formation of such intermediate-type margins has previously been reported (for example, the Gulf of California[12] and Red Sea[13]), but not confirmed by drilling.

Tectonic setting of the SCS oceanic basin

The SCS oceanic basin formed during the early Oligocene to middle Miocene (32–15 Ma)[14,15]. Its development includes the formation of several sub-basins (Fig. 1a) and rift propagation events. Our study focuses on an ~100-km-long segment[16] at the northern SCS margin within the northwest oceanic sub-basin (Fig. 1b). Previous studies have suggested major rifting during late Eocene time and final breakup during the early Oligocene[14,17]. Earlier extension events have been suggested based on pre-late Eocene, non-marine sediments within the deep part of the Pearl River Mouth Basin[17,18] located on the inner part of the ~400-km-wide SCS margin (Fig. 1a). However, evidence for major pre-late Eocene rifting in the distal margin of the SCS is neither supported by seismic data (Figs. 1b and 2a) that show only a single, strong rifting event, nor recovered by drilling. Our drilling study covers this distal ~200-km-wide margin where continental breakup took place, and extends seawards from the deep Liwan Basin to the oceanic crust (Figs. 1b and 2a). This specific margin segment has been interpreted as magma-poor, possibly hosting exhumed lower crust and upper mantle in its distal parts[16,19]. The conjugate Palawan margin (Fig. 1) is much less constrained, but a late Eocene to early Oligocene rifting across a 150–200 km zone is reported[20]. Widespread, possibly plume-related post-spreading magmatism across the margin[21,22] remains conjectural in light of our findings.

General structure of the northern SCS margin

The Liwan Basin is characterized by highly thinned crust, ≤10 km below the deepest rift basins (Fig. 2a), that formed in response to extensive normal faulting[4,17]. A major rifting event involving detachment faults can be identified from the seismic data, ending at or shortly after unconformity T80 (~30 Ma, Fig. 2a) with only minor post-breakup faults affecting unconformity T60 (~26 Ma). Most

A full list of affiliations appear at the end of the paper.

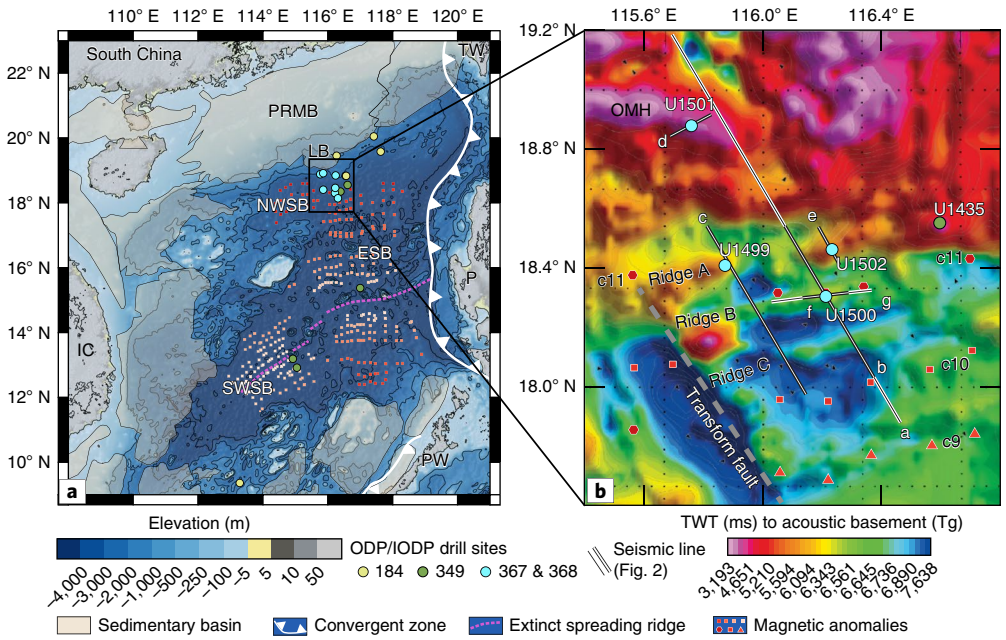

Fig. 1 | Regional setting and key basement topography of study area. a, Topographic map and major features of the SCS[49] with the location of IODP/ODP sites[14,16,50,51]. Sedimentary basins: Pearl River Mouth Basin (PRMB), Liwan Basin (LB). Ocean sub-basins: Eastern Sub-Basin (ESB), North West Sub-Basin (NWSB), South West Sub-Basin (SWSB). Continental domains: Indochina (IC), Palawan (PW), Philippines (P), Taiwan (TW). **b**, Depth to acoustic basement (Tg) presented with the seismic lines[16] used in Fig. 2 and indication of distinct topographic features: Outer Margin High (OMH) and Ridges A, B and C. Note the presence of a transform fault west of the margin segment being investigated. For both maps, picking of magnetic anomalies are after refs [26,52] with the geomagnetic timescale of ref. [53]. Gridded magnetic data are provided in refs [26,54].

major extensional faults sole out within a major decollement zone at the mid- to top of lower-crustal level (Fig. 2a). The Liwan Basin is bounded to the southeast by the Outer Margin High (OMH). The major decollement zone is interpreted to continue laterally below the OMH, but cannot be followed with confidence seaward of the OMH (Fig. 2a). The lower crust is thinnest (~8 km) beneath the deep rift basins, but thickens below, and possibly seawards of the OMH, suggesting that the lower crust remained ductile and able to flow during rifting, as also observed in previous studies[23,24]. Lower crustal flow may have continued beyond final breakup and caused local post-rift margin deformation[25].

Three distinct parallel basement ridges (A, B and C) trending west-southwest to east-northeast are present at the most distal margin (Figs. 1b, 2a–c and Supplementary Information) between 115° 40′ E and 116° 40′ E. Ridge A shows significant morphological variation (depth, width, reflection character) along strike, and sub-acoustic basement (Tg) reflectors cannot be regionally interpreted with any confidence (Fig. 2a–c,e). However, the continental Moho can be followed to and below Ridge A where the crust is only 2–2.5 s (two-way travel time (TWT); ~7–9 km) thick (Fig. 2a–c).

Ridges B and C are well defined by seawards-dipping bounding faults offsetting Tg, and show remarkable lateral continuity and smooth basement surfaces (Figs. 1b, 2a–c,f,g and Supplementary Information). Magnetic normal anomaly C11n (~29.5 Ma; Fig. 1)[26,27] is located close to Ridge B. Ridge C is within reverse magnetic anomaly C10r (~28.8–29.4 Ma) and C10n (~28.7 Ma) is placed seaward of it (Figs. 1b and 2a–c), implying an initial seafloor half-spreading rate of ~2.5 cm yr^{-1} (refs [26,27]).

In contrast to the continental Moho reflector below Ridge A, the Moho reflector beneath Ridges B and C is more patchy, although its depth is consistent with regional wide-angle seismic data[28] that show ~6-km-thick crystalline crust with $V_p > 5$ km s^{-1} from this location and seawards into younger oceanic crust. Crustal seismology and magnetic anomalies therefore suggest that the transition from continental crust to full oceanic crust is located between Ridge A and Ridge C.

Drilling results and correlation to seismic data

IODP Site U1501 on the crest of the OMH (Fig. 2a,d) recovered two lithostratigraphic units above the acoustic basement reflector Tg[29]. These two units are separated by unconformity T60 (~26 Ma) and they span the entire syn- and post-rift basin development: Unit 1 of early Miocene to Pleistocene age contains deep marine calcareous-rich sediment and ooze, and Unit 2 comprises late Eocene to late Oligocene siliciclastic sediments (Fig. 3)[29]. The base of the ~300-m-thick Unit 2 contains coarse sand intervals (shallow marine) with up to pebble-sized clasts, interbedded with millimetre-thin beds of lignite or coal and glauconite-bearing sand. Up-section, it shows overall fining of clastic material reflecting deepening basin conditions from (base) shallow marine to (top) bathyal depths. An age datum at the Eocene/Oligocene boundary (~34 Ma) located 200 m above the base of this Unit 2 suggests a late Eocene age for its deepest part. This is supported by similar sedimentary facies development of the deeper part of Unit 2 and the late Eocene Enping Formation recovered by industry boreholes within the Pearl River Mouth Basin[30], and is interpreted as reflecting the main SCS rifting event[17]. Site U1435[31] near the continent–ocean transition (Fig. 1) recovered similar ages and types of syn-rift sediments. It is noteworthy, however, that neither seismic data, nor coring data, show the presence of a distinct breakup unconformity within Unit 2. In particular, the T80 reflector (~30 Ma) is only represented in the cores by an upwards increase in calcareous nanno-fossils within the siliciclastic clay dominating T83-T80 interval. A marked change in the ratio between pelagic and benthic foraminifers upwards from T80 suggests basin deepening from shelf slope to bathyal depths[29] following final breakup within the most distal margin.

The material recovered from below the highly reflective Tg reflector is a strongly lithified sandstone to conglomerate displaying a sharp, major increase in density and P-wave velocities, and a sudden decrease in porosity (~20% to ~5%)[29]. An angular unconformity at Tg of about 15° is observed in the cores, and seismic data show a nearby, strong erosional truncation of a syncline (Fig. 2d

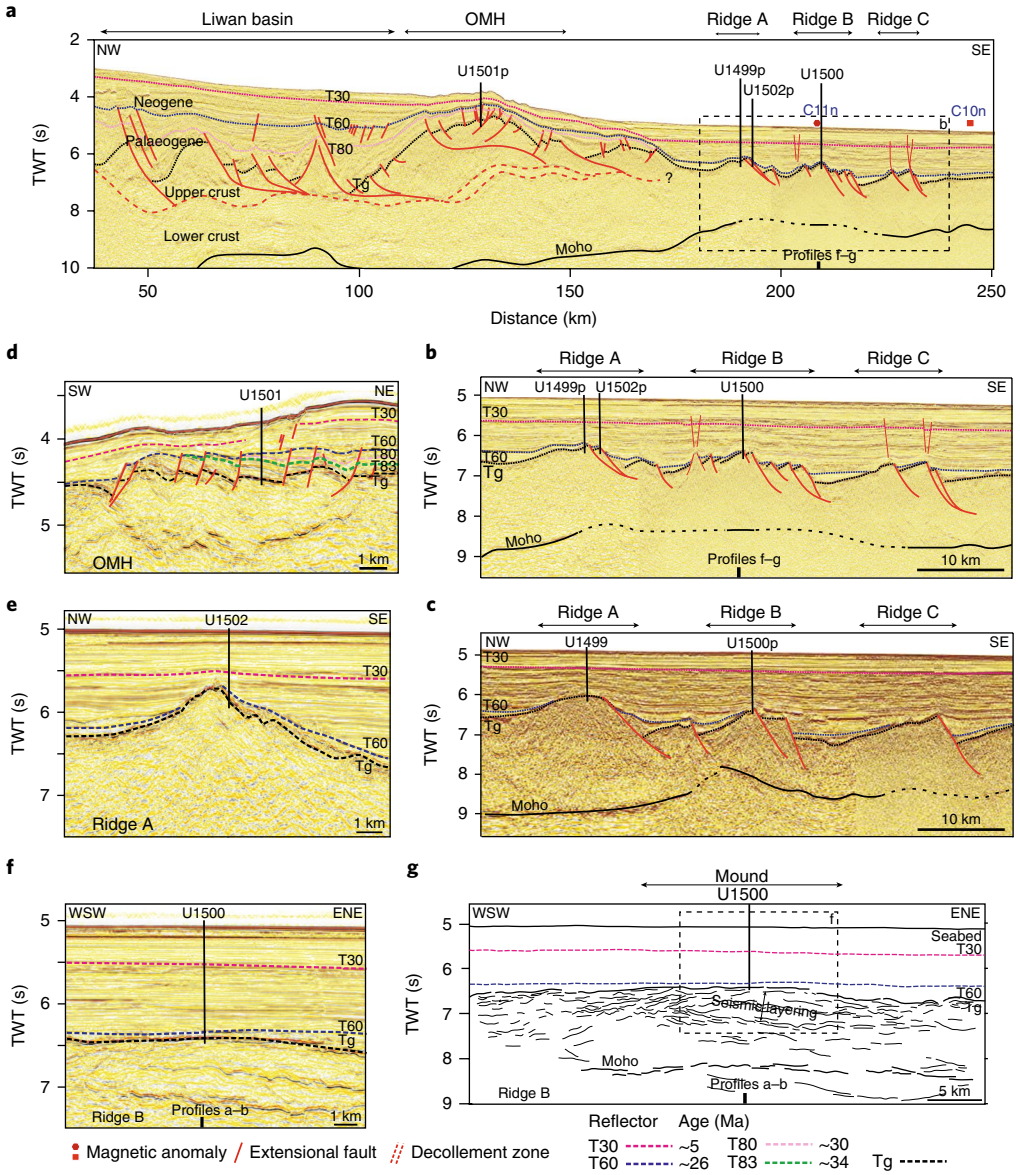

Fig. 2 | Interpreted seismic sections. For location of sections see Fig. 1. Drill sites marked with 'p' are projected. **a**, Regional seismic profile crossing the northern SCS margin. **b**,**c**, Expanded views of Ridges A, B and C, emphasizing their lateral continuity. **d**–**f**, Seismic sections across the drilling sites. **g**, Line drawing from a strike line across Ridge B showing a mound-like structure below Site U1500, suggesting that slightly younger volcanic strata may subcrop elsewhere along the ridge. Seismic data are taken and modified from refs [16,51]. The Chinese National Offshore Oil and Gas Company (CNOOC) convention for naming seismic stratigraphic unconformities[55,56] has been adapted. Regional seismic stratigraphic unconformities T30–T83 with ages are obtained from IODP drill cores. The T60 unconformity reflects some late, post rift deformation of minimal extension, possibly related to lower crustal flow[25]. Tg: acoustic basement does not represent a time line or specific stratigraphic relationships of lithologies (Fig. 3). Black line: Moho reflector (verified directly below Ridge B by wide-angle data[28]).

and Supplementary Information). Together, these factors imply that Tg represents a major hiatus between sediments suffering pre-rift deformation and compaction (Cretaceous?), and deposition of the overlying syn-rift deposits (Unit 2).

IODP Sites U1499 and U1502 sampled Ridge A (Fig. 2a–c,e), but yielded widely different results. The lower intervals of Site U1499[32] (Fig. 3) consist, from top to bottom, of (1) post-rift, lower Miocene fine-grained red claystone, (2) coarse siliciclastic sediments composed of a sandy matrix-supported breccia with angular pebble-sized sedimentary clasts bearing ages spanning from early Miocene (~23 Ma) through early Oligocene (~30 Ma)[32], (3) undated, moderately lithified gravel composed mostly of polygenic cobble-sized clasts. The clasts predominantly consist of previously eroded sedimentary rocks (mostly coarse-grained sandstone).

Site U1502 is located 40 km east of Site U1499 along Ridge A (Figs. 1 and 2e). In the seismic profiles (Fig. 2e), a highly reflective Tg is dipping ~25°, and is overlain by moderately dipping to sub-horizontal onlapping sedimentary layers of mainly post-rift age. Below Tg, a total of 180 m of basaltic lavas with pillow structures were recovered, and are immediately overlain (Fig. 3) by a condensed sequence of fine-grained, deep-marine sediments ranging in age from early Oligocene (~30 Ma) to early Miocene (~23 Ma)[33]. Clay to claystone immediately above the basalts documents an assemblage of agglutinated benthic foraminifers that, if indeed in situ material, could indicate a late Eocene age[33].

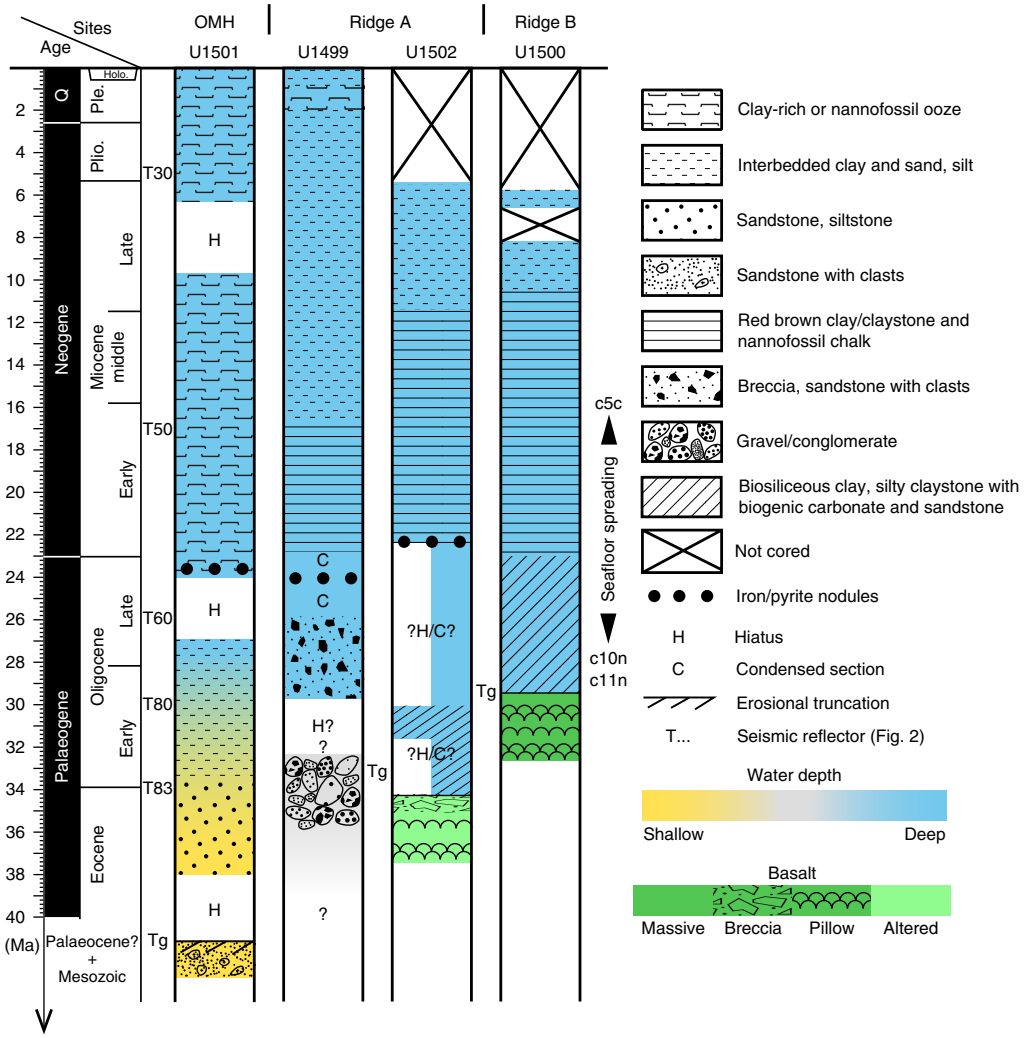

Fig. 3 | Summary chart of drilling results. Ages based on core samples analysed for calcareous nannofossils, foraminifers, diatoms and ostracods. Lithostratigraphy is from detailed core descriptions[29,32–34] following the GTS12[48] geological timescale.

The entire basalt sequence suffered pervasive hydrothermal alteration reaching greenschist facies conditions and profound brecciation (hydro-fracturing) associated with abundant iron sulfide mineralization[33]. This hydrothermal activity extends into the lowermost part (~5 m) of the overlying, deep-marine sediments of early Oligocene age (Fig. 3), implying that no major hiatus exists between igneous activity and sedimentation. This effectively constrains the basaltic activity in late Eocene–early Oligocene time (~30–34 Ma) during the final stages of continental breakup. The strong and seaward rotation differs from that of Ridge B (~5° landward rotation), and is consistent with late-stage deformation at the most distal continental margin before the onset of margin-wide magmatism at Ridge B.

Continuation of the continental Moho (Fig. 2a–c) below Ridge A implies that this ridge is floored by continental crust. There is no indication of magmatism at Site U1499 at the time of continental breakup. Instead, matrix-supported breccia and gravels were recovered at Site U1499 below Tg, and possibly were deposited by syntectonic gravity flows in response to rifting. The gravels have a large proportion of upper crustal materials, in part of sedimentary origin, suggesting limited, if any, deep tectonic exhumation in the source area. Overall, this suggests that Ridge A records the interplay between late-stage continental extension and breakup-related magmatism.

Site U1500 on the landwards tilted (~5°) fault block of Ridge B (Fig. 2f,g) recovered 1,380 m of deep marine Neogene to Oligocene

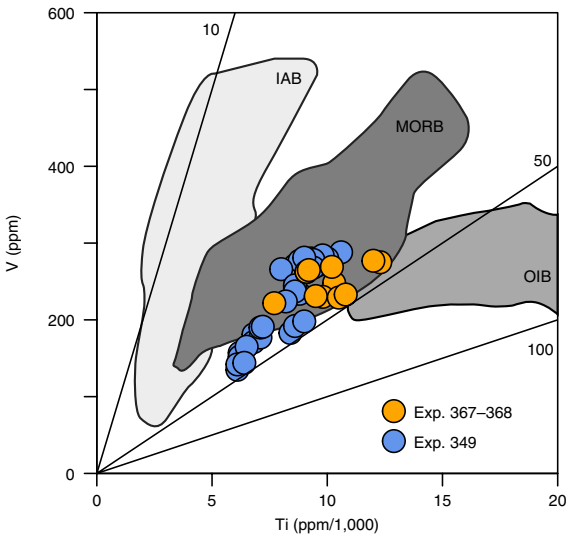

Fig. 4 | Geochemical discrimination diagram. Titanium (Ti) and vanadium (V) content[57] of basalts sampled by IODP expeditions 367–368 on the rifted margin (Sites U1500 and U1502)[33,34] and IODP 349 sites located on oceanic crust[14]. See Supplementary Material 3. IAB, island arc basalts; MORB, mid-ocean ridge basalts; OIB, ocean island basalts.

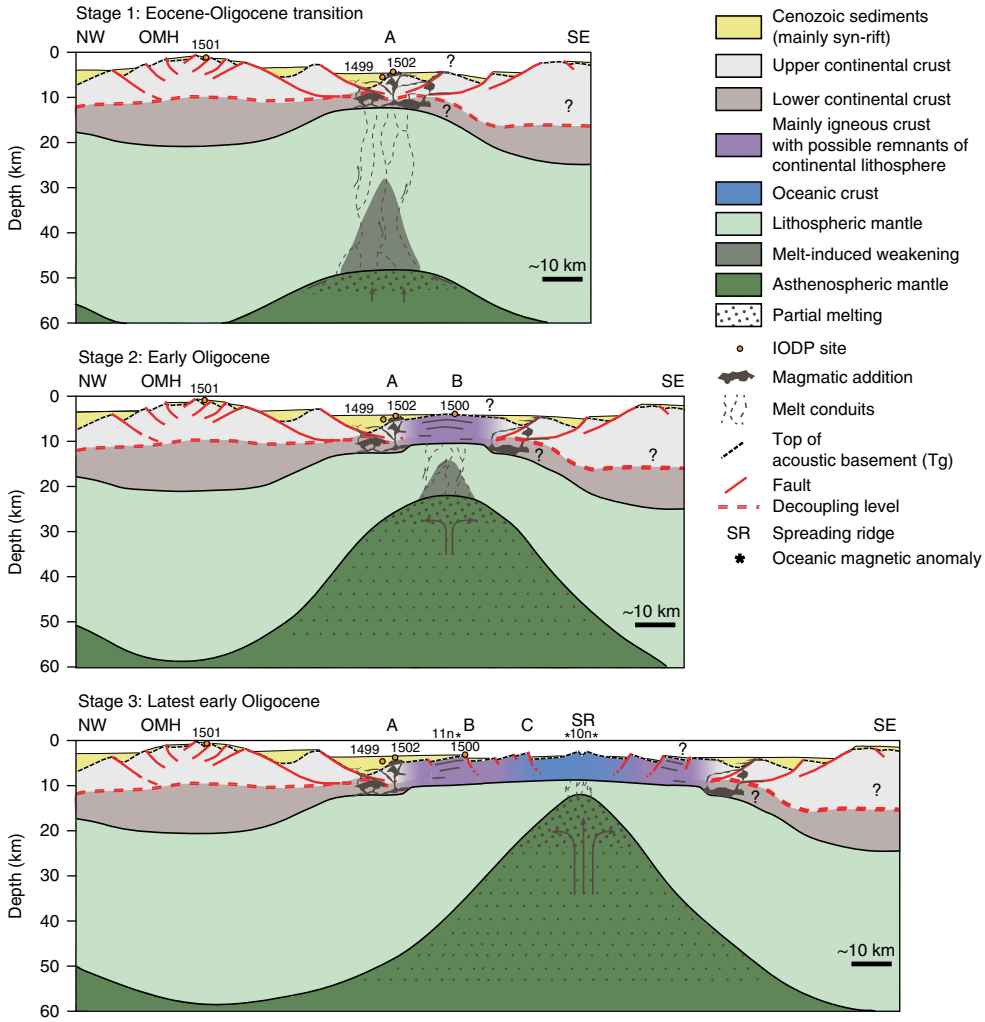

Fig. 5 | Conceptual model of continental breakup based on integration of seismic and drilling data from Figs. 2 and 3. Stage 1: a deep basin with thin crust existed within the final zone of plate rupture and hosted magmatism at the Eocene–Oligocene transition, based on Site U1502 findings. Stage 2: ascending melts rapidly weakened the mantle lithosphere, and massive extrusive activity along the entire rift zone took place, underpinned by a thicker zone of melting in the asthenosphere. Stage 3: seafloor spreading and passive upwelling of asthenospheric mantle was established. Igneous basement of Ridges B and C was affected by normal faults. Note that, in time, stages 2 and 3 are ~1 Myr apart (or less), but a high rate (~2.5 cm yr^{-1}, half-rate) of plate separation translates to significant distance in space. The area of possible transient crust around Ridge B is shown in purple. Constraints on the southern conjugate margin (Palawan) structure are limited to seismic data of moderate quality[20] and only schematically represented. However, both the timing of rifting at the distal margin and the width of the zone of main crustal necking are similar on both margins.

sediments overlying 150 m of volcanic basement[34]. The fresh to moderately altered basaltic lavas alternate between thick massive flows and pillow flows (Fig. 3). Very thin intercalated sediment layers are present within the lavas. Nannofossils of Oligocene age within these sediments are consistent with the presence of upper Oligocene to lower Miocene post-basaltic sediments, and with the alignment of magnetic chron C11n (29.5 Ma) with Ridge B (Figs. 1, 2a–c and 3).

The along-ridge seismic line shows that the basement sampled at Site U1500 is acoustically layered down to ~2 km below Tg (V_p of 4.5–5.0 km s^{-1}) in a similar fashion as the cored upper 150 m, and this extends all along Ridge B (Fig. 2f,g and Supplementary Information). This suggests that an ~2-km-thick (minimum) volcanic edifice is present at this ridge. Although this implies considerable basaltic magmatism along the entire Ridge B around Chron C11n time, it does not unambiguously prove that full oceanic crust is present below Ridge B. A thick extrusive cover might be sufficient to generate the magnetic anomaly, even if it is floored by remnants of continental lithosphere. Ridge B, however, shares the characteristic features of Ridge C (as opposed to the continental Ridge A), which, except for its fault-bounded nature, forms a straight continuation into the younger SCS oceanic crust.

Importantly, the composition of the basalts from ridges A and B forms a continuum with that of the igneous oceanic crust sampled by IODP expedition 349 within the younger SCS basin[14]. Sites U1500 and U1502 lavas all have MORB (Mid-Ocean Ridge Basalt) compositions (Fig. 4) with MORB-like petrography: plagioclase phyric, olivine-bearing, lacking clinopyroxene phenocrysts. This is consistent with mantle-derived primitive, dry melts, generated by decompression melting in a mid-ocean-ridge setting. From this, we conclude that a melting regime comparable to a mature spreading centre in terms of melt composition, productivity and lateral extent was present during the time of final rifting and breakup (Ridge A to Ridge B stage) and continued to operate during the subsequent SCS formation (Ridge C and younger).

The normal faults of Ridges B and C show significant displacements (up to ~500 m) of Tg representing igneous basement and the very oldest post-breakup sediments, but do not offset the younger sediments of latest Oligocene to early Miocene sediments. This fault activity therefore occurred within a short time interval (mid-Oligocene)

during or just after the formation of the igneous basement and is, in this regard, reminiscent of abyssal hill-type topography. The modest (~5°) block rotation, however, suggests that only minor tectonic extension operated in tandem with the igneous crustal accretion during final breakup to early seafloor spreading.

Breakup model for the northern SCS margin

A major rifting event of late Eocene to early Oligocene age on the outer, distal margin of the northern SCS is suggested by both seismic observations and Site U1502 cores. The drilling data support a kinematic history of the SCS with breakup at around magnetic chron C11n (~30 Ma), but the finding of extensive MORB-type magmatism at final breakup time contradicts previous studies that suggested a magma-poor margin involving mantle exhumation and magma starvation[19]. Similarly, cores show no evidence for the late-stage, post breakup magmatism hypothesized to overprint the margin[21].

Combined with seismic data, the drilling results strongly suggest that Ridge A is floored by continental crust, but locally experienced MORB magmatism within its eastern part (that is, Site U1502), potentially reflecting an east to west propagation of initial margin magmatism. The age of this magmatism is constrained to be between late Eocene to early Oligocene (30 Ma to possibly 34 Ma). Ridge B, in contrast, has a ridge-long cover of at least 2-km-thick volcanics (MORB-type) of early Oligocene age (Figs. 2g and 3), aligns with the magnetic Chron C11n anomaly (~30 Ma), and is in most aspects comparable to Ridge C. However, it cannot be excluded that Ridge B represents transitional crust (Fig. 5), as opposed to the mature oceanic igneous crust that subsequently formed. This uncertainty in the location of the rift-to-drift transition is only ~20 km (Stages 2–3, Fig. 5) and equivalent to ~1 Myr in time (assuming an average half-extension rate of 2 cm yr^{-1} or higher between ridges A and C).

A key characteristic of the northern SCS margin revealed by the IODP cores, therefore, is a relatively short (<10 Myr) rifting event with a narrow, and by implication, rapid rift-to-igneous crustal accretion transition. This is in marked contrast with the magma-poor Iberia–Newfoundland margins recording more than ~30 Myr of crustal rifting and extensive (>100 km) subcontinental mantle exhumation prior to igneous crustal accretion[10,11,35,36].

Establishment of a mantle-melting regime yielding MORB-type magmatism at, or even slightly before (Site U1502), final breakup is readily explained at magma-rich margins by emplacement of anomalously hot asthenosphere[6,37]. However, the lack of the distinct characteristics of magma-rich margins at the SCS implies the need for a different model for this margin. Instead, we suggest that rifting of the SCS margin, involving a major and fast episode of extension during late Eocene to early Oligocene time, enabled formation of sufficient decompression melting within the asthenosphere to initiate the passive asthenospheric upwelling eventually needed to form full igneous crust from normal-temperature mantle (Fig. 5). Assuming an original crustal thickness of ~30 km, the only ~8-km-thick residual continental crust below Ridge A implies a stretching factor of ~4. Normal-temperature asthenospheric mantle can in this case lead to significant melt production[38,39]. For Ridge B, where residual continental crust is ~4 km or less, melt supply could be very high and approach that of full oceanic crust. However, in addition to the amount of stretching, rift duration also has profound impact on melt yields[40]. High extension rates imply fast vertical ascent of asthenospheric mantle that suppresses heat loss through conduction and, provided focused upwelling takes place, normal thickness oceanic crust can form[39,40]. The relatively high rate of spreading recorded in the SCS after breakup (2.5 cm yr^{-1}, half rate) exceeds the threshold ascent rate of ~1 cm yr^{-1} considered a limit for effective supply of crust-forming melts during steady-state spreading[41].

If we further consider that the SCS margin formed within relatively young and hot lithosphere[23,24] with a thickness (present day) of only 80 km[42], melt generation would initiate at lower stretching factors compared to normal conditions[40]. Ascent of early melts (Fig. 5) provides for convective heat transfer into the lithosphere[43,44], can favour grain boundary sliding leading to reduced viscosity[45], and effectively aids extension and rift localization during late-stage rifting[13]. The decoupling of extension between crust and mantle by a ductile lower crust may have contributed to this process by allowing the mantle lithosphere to extend independently of the crust in both time and space[13,23,46]. The presence of a relatively thin pre-breakup lithosphere is independently supported by modelling of the anomalously high heat flow (~100 mW m^{-2}, Sites 1499 and 1501[29,32]) characterizing the margin[47].

In summary, a major rifting event within thin lithosphere permitted mantle upwelling, yielding abundant MORB-type melts during final breakup and early seafloor spreading, and resulted a narrow and fast rift-to-drift transition along the northern SCS.

Methods

Methods, including statements of data availability and any associated accession codes and references, are available at https://doi.org/10.1038/s41561-018-0198-1.

Received: 11 November 2017; Accepted: 4 July 2018;
Published online: 20 August 2018

References

1. Peron-Pinvidic, G., Manatschal, G. & Osmundsen, P. T. Structural comparison of archetypal Atlantic rifted margins: a review of observations and concepts. *Mar. Pet. Geol.* **43**, 21–47 (2013).
2. Tugend, J. et al. *Reappraisal of the Magma-Rich versus Magma-Poor Rifted Margin Archetypes* Spec. Pub. SP476.9 (Geological Society of London, 2018); https://doi.org/10.1144/SP476.9
3. Franke, D. Rifting, lithosphere breakup and volcanism: comparison of magma-poor and volcanic rifted margins. *Mar. Pet. Geol.* **43**, 63–87 (2013).
4. Gao, J. et al. The continent–ocean transition at the mid-northern margin of the South China Sea. *Tectonophysics* **654**, 1–19 (2015).
5. Lester, R. et al. Rifting and magmatism in the northeastern South China Sea from wide-angle tomography and seismic reflection imaging. *J. Geophys. Res. Solid Earth* **119**, 2305–2323 (2014).
6. Holbrook, W. S. et al. Mantle thermal structure and active upwelling during continental breakup in the North Atlantic. *Earth Planet. Sci. Lett.* **190**, 251–266 (2001).
7. Larsen, H. C. & Saunders, A. D. Tectonism and volcanism at the southeast greenland rifted margin: a record of plume impact and later continental rupture. In *Proc. ODP Sci. Res.* (eds Saunders, A. D., Larsen, L. C. & Wise, S. W. Jr) Vol. 152, Ch. 41 (ODP, 1998); https://doi.org/10.2973/odp.proc.sr.152.240.1998
8. Boillot, G., Winterer, E. L. & Al, E. Drilling on the galicia margin: retrospect and prospect. In *Proc. ODP Sci. Res.* (eds Boillot, G., Winterer, E. L. & Meyer, A. W.) Vol. 103, Ch. 45 (ODP, 1988); https://doi.org/10.2973/odp.proc.sr.103.180.1988
9. Minshull, T. A. Geophysical characterisation of the ocean–continent transition at magma-poor rifted margins. *Comptes Rendus Geosci.* **341**, 382–393 (2009).
10. Tucholke, B. & Sibuet, J.-C. Leg 210 synthesis: tectonic, magmatic, and sedimentary evolution of the newfoundland-iberia rift. In *Proc. ODP Sci. Res.* (eds Tucholke, B.E., Sibuet, J.-C. & Klaus, A) Vol. 210, Ch. 1 (ODP, 2007); https://doi.org/10.2973/odp.proc.sr.210.101.2007
11. Whitmarsh, R. B., Manatschal, G. & Minshull, T. A. Evolution of magma-poor continental margins from rifting to seafloor spreading. *Nature* **413**, 150–154 (2001).
12. Lizarralde, D. et al. Variation in styles of rifting in the Gulf of California. *Nature* **448**, 466–469 (2007).
13. Ligi, M. et al. Birth of an ocean in the Red Sea: initial pangs. *Geochem. Geophys. Geosyst.* **13**, Q08009 (2012).
14. Li, C.-F., Lin, J., Kulhanek, D. K. & Expedition 349 Scientists. Expedition 349 summary. In *Proc. IODP* (eds Li, C.-F., Lin, J., Kulhanek, D. K. & Expedition 349 Scientists) Vol. 349, Ch. 1 (IODP, 2015); https://doi.org/10.14379/iodp.proc.349.101.2015
15. Taylor, B. & Hayes, D. Origin and history of the South China Sea basin. *Tecton. Geol. Evol.* **27**, 23–56 (1983).
16. Sun, Z. et al. *Expedition 367/368 Scientific Prospectus: South China Sea Rifted Margin* 39–106 (IODP, 2016); https://doi.org/10.14379/iodp.sp.367368.2016

17. Zhou, D., Ru, K. & Chen, H. Kinematics of Cenozoic extension on the South China Sea continental margin and its implications for the tectonic evolution of the region. *Tectonophysics* **251**, 161–177 (1995).
18. Ru, K. & Pigott, J. D. Episodic rifting and subsidence in the South China Sea. *Am. Assoc. Pet. Geol. Bull.* **70**, 1136–1155 (1986).
19. Franke et al. The final rifting evolution in the South China Sea. *Mar. Pet. Geol.* **58**, 704–720 (2014).
20. Franke, D. et al. The continent-ocean transition at the southeastern margin of the South China Sea. *Mar. Pet. Geol.* **28**, 1187–1204 (2011).
21. Fan, C. et al. New insights into the magmatism in the northern margin of the South China Sea: spatial features and volume of intraplate seamounts. *Geochem. Geophys. Geosyst.* **18**, 2216–2239 (2017).
22. Zhao, F. et al. Prolonged post-rift magmatism on highly extended crust of divergent continental margins (Baiyun Sag, South China Sea). *Earth Planet. Sci. Lett.* **445**, 79–91 (2016).
23. Brune, S., Heine, C., Clift, P. D. & Pérez-Gussinyé, M. Rifted margin architecture and crustal rheology: reviewing Iberia–Newfoundland, Central South Atlantic, and South China Sea. *Mar. Pet. Geol.* **79**, 257–281 (2017).
24. Clift, P., Lin, J. & Barckhausen, U. Evidence of low flexural rigidity and low viscosity lower continental crust during continental break-up in the South China Sea. *Mar. Pet. Geol.* **19**, 951–970 (2002).
25. Clift, P. D., Brune, S. & Quinteros, J. Climate changes control offshore crustal structure at South China Sea continental margin. *Earth Planet. Sci. Lett.* **420**, 66–72 (2015).
26. Briais, A., Patriat, P. & Tapponnier, P. Updated interpretation of magnetic anomalies and seafloor spreading stages in the south China Sea: implications for the Tertiary tectonics of Southeast Asia. *J. Geophys. Res.* **98**, 6299 (1993).
27. Li, C.-F. et al. Ages and magnetic structures of the South China Sea constrained by deep tow magnetic surveys and IODP Expedition 349. *Geochem. Geophys. Geosyst.* **15**, 4958–4983 (2014).
28. Pin, Y., Di, Z. & Zhaoshu, L. A crustal structure pro file across the northern continental margin of the South China Sea. *Tectonophysics* **338**, 1–21 (2001).
29. Larsen, H. C. et al. Site U1501. In *Proc. IODP* (eds Sun, Z. et al.) Vol. 367/368, Ch. 5 (IODP, 2018); https://doi.org/10.14379/iodp.proc.367368.105.2018
30. Pinglu, L. & Chuntao, R. Tectonic characteristics and evolution history of the Pearl river mouth basin. *Tectonophysics* **235**, 13–25 (1994).
31. Li, C.-F., Lin, J., Kulhanek, D. K. & Expedition 349 Scientists. Site U1435. In *Proc. IODP* (eds Li, C.-F., Lin, J., Kulhanek, D. K. & Expedition 349 Scientists) Vol. 349, Ch. 7 (IODP, 2015); https://doi.org/10.14379/iodp.proc.349.107.2015
32. Sun, Z. et al. Site U1499. In *Proc. IODP* (eds Sun, Z. et al.) Vol. 367/368, Ch. 3 (IODP, 2018); https://doi.org/10.14379/iodp.proc.367368.103.2018
33. Larsen, H. C. et al. Site U1502. In *Proc. IODP* (eds Sun, Z. et al.) Vol. 367/368, Ch. 6 (IODP, 2018); https://doi.org/10.14379/iodp.proc.367368.106.2018
34. Stock, J. M. et al. Site U1500. In *Proc. IODP* (eds Sun, Z. et al.) Vol. 367/368, Ch. 4 (IODP, 2018); https://doi.org/10.14379/iodp.proc.367368.104.2018
35. Minshull, T. A., Dean, S. M., White, R. S. & Whitmarsh, R. B. Anomalous melt production after continental break-up in the southern Iberia Abyssal Plain. *Geol. Soc. Lond., Spec. Publ.* **187**, 537–550 (2001).
36. Mohn, G., Karner, G. D., Manatschal, G. & Johnson, C. A. Structural and stratigraphic evolution of the Iberia–Newfoundland hyper-extended rifted margin: a quantitative modelling approach. *Geol. Soc. Lond. Spec. Pub.* **413**, 53–89 (2015).
37. White, R. & McKenzie, D. Magmatism at rift zones: the generation of volcanic continental margins and flood basalts. *J. Geophys. Res.* **94**, 7685 (1989).
38. Fletcher, R., Kusznir, N. & Cheadle, M. Melt initiation and mantle exhumation at the Iberian rifted margin: comparison of pure-shear and upwelling-divergent flow models of continental breakup. *Comptes Rendus Geosci.* **341**, 394–405 (2009).
39. Mckenzie, D. & Bickle, M. J. The volume and composition of melt generated by extension of the lithosphere. *J. Petrol.* **29**, 625–679 (1988).
40. Bown, J. W. & White, R. S. Effect of finite extension rate on melt generation at rifted continental margins. *J. Geophys. Res. Solid Earth* **100**, 18011–18029 (1995).
41. Lizarralde, D., Gaherty, J. B., Collins, J. A., Hirth, G. & Kim, S. D. Spreading-rate dependence of melt extraction at mid-ocean ridges from mantle seismic refraction data. *Nature* **432**, 744–747 (2004).
42. Yu, C. et al. Deep thermal structure of Southeast Asia constrained by S-velocity data. *Mar. Geophys. Res.* **38**, 341–355 (2017).
43. Sotin, C. & Parmentier, E. M. Dynamical consequences of compositional and thermal density stratification beneath spreading centers. *Geophys. Res. Lett.* **16**, 835–838 (1989).
44. McKenzie, D. P. The generation and compaction of partial melts. *J. Petrol.* **25**, 713–765 (1984).
45. Ohuchi, T. et al. Dislocation-accommodated grain boundary sliding as the major deformation mechanism of olivine in the Earth's upper mantle. *Sci. Adv.* **1**, e1500360 (2015).
46. Huismans, R. & Beaumont, C. Depth-dependent extension, two-stage breakup and cratonic underplating at rifted margins. *Nature* **473**, 74–78 (2011).
47. Nissen, S. S. et al. Gravity, heat flow, and seismic constraints on the processes of crustal extension: northern margin of the South China Sea. *J. Geophys. Res.* **100**, 22447 (1995).
48. Gradstein, F. M. & Ogg, J. G. in *The Geologic Time Scale* (eds Gradstein, F. M., Ogg, J. G., Schmitz, M. D. & Ogg, G. M.) Ch. 2, 31–42 (Elsevier, Amsterdam, 2012).
49. Amante, C. & Eakins, B. W. *ETOPO1 1 Arc-Minute Global Relief Model: Procedures, Data Sources and Analysis* NOAA Tech. Memo NESDIS NGDC-24 (National Geophysical Data Center, NOAA, 2009); https://doi.org/10.1594/PANGAEA.769615
50. Wang, P., Prell, W. L. & Blum, P. (eds) in *Proc. ODP, Init. Repts* Vol. 184, Ch. 1 (ODP, 2000).
51. Larsen, H. C. et al. Expedition 367/368 summary. In *Proc. IODP* (eds Sun, Z. et al.) Vol. 367/368, Ch. 1 (IODP, 2018); https://doi.org/10.14379/iodp.proc.367368.101.2018
52. Seton, M. et al. Community infrastructure and repository for marine magnetic identifications. *Geochem. Geophys. Geosyst.* **15**, 1629–1641 (2014).
53. Gee, J. S. & Kent, D. V. Source of oceanic magnetic anomalies and the geomagnetic polarity timescale. *Treatise Geophys.* **5**, 455–507 (2007).
54. Ishihara, T. & Kisimoto, K. *Magnetic Anomaly Map of East Asia 1:4.000.000, CD-ROM* (Geological survey of Japan, 1996).
55. Dai, Y. et al. Threshold conditions and reservoir-controlling characteristics of source kitchen in Zhu I depression, Pearl River Mouth Basin. *Acta Pet. Sin.* **36**, 145–155 (2015).
56. Shi, H., He, M. & Zhang, L. Hydrocarbon geology, accumulation pattern and the next exploration strategy in the eastern Pearl River Mouth basin. *China Offshore Oil Gas.* **26**, 11–22 (2014).
57. Shervais, J. W. Ti–V plots and the petrogenesis of modern and ophiolitic lavas. *Earth Planet. Sci. Lett.* **59**, 101–118 (1982).

Acknowledgements

The authors acknowledge the Chinese National Offshore Oil and Gas Company (CNOOC) for providing access for Z.S. and H.C.L. to work on their large regional database of seismic reflection data, which CNOOC subsequently amended with acquisition of new data to document our selected drill sites. The authors thank the RV *JOIDES Resolution* crew and the IODP technical staff. The IODP–China office supported international workshops to develop the original drilling proposal. Co-principal investigators of the drilling proposal, P. Wang and C.-F. Li, are acknowledged for their contributions to planning. This research used data and samples provided by the International Ocean Discovery Program. A.K. and C.A.-Z. acknowledge support from NSF award no. OCE-1326927. D.Z. was supported by the Korean IODP program (KIODP).

Author contributions

H.C.L. was co-principal investigator (co-PI) for the original drilling proposal and interpretation of seismic data, co-chief scientist of expeditions 367/368, and directed the writing of the paper. G.M. is principal co-author, developed the geodynamic model jointly with H.C.L. and M.N. and was a shipboard scientist (structural geology) at expedition 368. M.N. was a shipboard scientist (structure/sedimentology) at expedition 367, carried out structural interpretation of syn-rift sedimentation, and contributed to model development and graphics. Z.S was co-PI for the original drilling proposal, interpretation of seismic data, and was co-chief scientist of expeditions 367/368. J.S. was co-chief scientist of expeditions 367/368 and co-proponent of the original drilling proposal. Z.J. was co-chief scientist of expeditions 367/368 and coordinated biostratigraphic interpretations. A.K. was expeditions 367/368 project manager. C.A.A.-Z. was expeditions 367/368 project manager and performed biostratigraphy. J.B., A.B., Y.C., M.D., A.F., J.H., T.W.H., K.H., B.H., X.H., B.J., C.Lei., L.L., Z.L., A.L., C.Lupi, A.McC., M.N., C.R., I.S., C.S., X.S., R.X., R.Y., L.Y., C.Z., J.Z., Y.Z., N.Z. and L.Z. collected the drilling data during IODP expedition 367 and participated in the writing of the paper. S.B., D.C., K.D., W.D., E.F., F.F., A.G., E.H., S.J., H.J., R.K., B.L., Y.L., J.L. (co-PI)., Chang Liu, Chuanlian Liu, L.N., N.O., D.W.P., P.P., N.Q., S.Sa., J.C.S., S.St., L.T., F.M.vdZ., S.W., H.W., P.S.Y. and G.Z. collected the drilling data during IODP expedition 368 and participated in writing of the paper. Roles on board are detailed in https://iodp.tamu.edu/scienceops/precruise/southchinasea2/participants.html.

Competing interests

The authors declare no competing interests.

Additional information

Supplementary information is available for this paper at https://doi.org/10.1038/s41561-018-0198-1.

Reprints and permissions information is available at www.nature.com/reprints.

Correspondence and requests for materials should be addressed to H.C.L. or G.M.

Publisher's note: Springer Nature remains neutral with regard to jurisdictional claims in published maps and institutional affiliations.

[1]State Key Laboratory of Marine Geology, Tongji University, Shanghai, China. [2]Geological Survey of Denmark and Greenland, Copenhagen, Denmark. [3]Université de Cergy-Pontoise, Laboratoire Géosciences et Environnement Cergy (GEC), Neuville-sur-Oise, France. [4]CAS Key Laboratory of Ocean and Marginal Sea Geology, South China Sea Institute of Oceanology, Guangzhou, China. [5]Division of Geological and Planetary Sciences, California Institute of Technology, Pasadena, CA, USA. [6]International Ocean Discovery Program, Texas A&M University, College Station, TX, USA. [7]Dipartimento di Geoscienze, Università degli Studi di Padova, Padova, Italy. [8]School of Geosciences, University of Aberdeen, Aberdeen, UK. [9]GET, Universite de Toulouse, UMR 5563 CNRS, CmNES, IRD, Obs. Midi-Pyrenees, Toulouse, France. [10]Guangzhou Institute of Geochemistry, Chinese Academy of Sciences, Guangzhou, China. [11]Petroleum & Marine Research Division, Korea Institute of Geoscience and Mineral Resources (KIGAM), Daejeon, Republic of Korea. [12]School of Geosciences, University of Sydney, Camperdown, New South Wales, Australia. [13]Key Laboratory of Submarine Geoscience, Second Institute of Oceanography (SIO), State Oceanic Administration (SOA), Hangzhou, China. [14]Department of Geological Sciences, Brigham Young University, Provo, UT, USA. [15]School of Geosciences, University of Louisiana at Lafayette, Lafayette, LA, USA. [16]Programa de Pós-Graduação em Dinâmica dos Oceanos e da Terra da Universidade Federal Fluminense (DOT-UFF), Brazil - CAPES Foundation, Ministry of Education of Brazil, Brasilia, Brazil. [17]Department of Geoscience, Shimane University, Matsue City, Shimane, Japan. [18]Earth and Atmospheric Sciences, University of Nebraska–Lincoln, Lincoln, NE, USA. [19]JAMSTEC, Yokohama, Kanagawa, Japan. [20]Department of Geology, Peking University, Beijing, China. [21]State Key Laboratory of Isotope Geochemistry, Guangzhou Institute of Geochemistry, Chinese Academy of Sciences, Guangzhou, China. [22]Institute of Groundwater and Earth Sciences, Jinan University, Guangzhou, China. [23]Department of Geology and Geography, West Virginia University, Morgantown, WV, USA. [24]GEOMAR Helmholtz Center for Ocean Research , Kiel, Germany. [25]Institute of Geosciences, Christian-Albrechts-Universität zu Kiel, Kiel, Germany. [26]Key Laboratory of Tectonics and Petroleum Resources of Ministry of Education, China University of Geosciences, Wuhan, China. [27]Department of Micropalaeontology, Nanjing Institute of Geology and Palaeontology, Nanjing, China. [28]School of Geographical and Oceanographical Sciences, Nanjing University, Nanjing Shi, China. [29]Department of Geology and Geophysics, Woods Hole Oceanographic Institution, Woods Hole, MA, USA. [30]Department of Geology and Geophysics, Louisiana State University, Baton Rouge, LA, USA. [31]Department of Geology, University of South Florida, Tampa, FL, USA. [32]Department of Earth and Environmental Sciences, Università degli studi di Pavia, Pavia, Italy. [33]Institute of Earth Sciences, University of Lausanne, Geopolis, Lausanne, Switzerland. [34]Department of Marine Geophysics, National Centre for Antarctic and Ocean Research (NCAOR), Vasco Da Gama, Goa, India. [35]Faculty of Science, Graduate School of Science and Technology for Innovation, Yamaguchi-shi, Yamaguchi, Japan. [36]Earth & Environmental Sciences, University of Iowa, Iowa City, IA, USA. [37]School of Earth Sciences, Ohio State University, Columbus, OH, USA. [38]Dipartimento di Ingegneria e Geologia, Università degli studi G D'Annunzio Chieti-Pescara, Chieti, Italy. [39]Institute for Marine and Antarctic Studies (IMAS), University of Tasmania, Hobart, Tasmania, Australia. [40]Institute of Earth Sciences, Heidelberg University, Heidelberg, Germany. [41]Department of Geology, California State University, Sacramento, CA, USA. [42]Lamont Doherty Earth Observatory of Columbia University, Palisades, NY, USA. [43]Institute of Oceanography, National Taiwan University, Tapei, Taiwan. [44]Institute of Deep-sea Science and Engineering, Chinese Academy of Sciences, Sanya City, Hanai Province, China. [45]Institute of Oceanology, Chinese Academy of Sciences, Qingdao, Shandong Province, China. [46]School of Ocean Sciences, China University of Geosciences, Haidian District, Beijing, China. [47]Taiwan Ocean Research Institute, NARLabs, Kaohsiung, Taiwan. [48]Department of Earth, Atmospheric and Planetary Sciences, Purdue University, West Lafayette, IN, USA. [49]School of Marine Sciences, Sun Yat-Sen University, Zhuhai, China. [50]Present address: School of Earth Sciences, University of Bristol , Clifton, UK. *e-mail: hclarseniodp@gmail.com; geoffroy.mohn@u-cergy.fr

Methods

All new data in this publication were produced onboard RV *JOIDES Resolution* during IODP expeditions 367 and 368, except for the seismic data (courtesy of CNOOC). The methods applied for all data types are described in detail in pages 1–67 of ref. [58]. All methods, data, sampling frequency and curatorial procedures can be retrieved, from 28 September 2018, via the *JOIDES Resolution* Science Operator web site (http://iodp.tamu.edu/scienceops/expeditions/south_china_sea_II.html). Methods of particular importance for this contribution relate to whole rock geochemistry, biostratigraphy and timescales, seismic data and their correlation to drill holes and cores.

Geochemical analysis. The fresh to moderately altered basalts and highly altered basalts sampled from sites U1500 and U1502, respectively, were analysed onboard for major and trace element concentrations during expeditions 367 and 368 using a Leeman inductively coupled plasma–atomic emission spectroscopy (ICP–AES) instrument. Samples were cut from the core with a diamond saw blade, removing altered rinds and surface contamination from the drill or saw. During expeditions 367 and 368, run-to-run relative standard deviation with ICP–AES was generally ±1% for the major elements, except for MgO (±5%) and ±10% for trace elements. The detailed ICP–AES procedure is described in the Methods section of ref. [58].

Stratigraphy and timescales. Stratigraphic and specific age constraints were established during IODP expeditions 367 and 368 using (1) biostratigraphy, (2) palaeomagnetic data, (3) sediment core description and lithostratigraphy, and (4) core and borehole petrophysical and geophysical measurements[17]. The timescale of Gradstein and Ogg[48] was used for reference. Biostratigraphic analyses were carried out for all core catcher samples. Additional samples were taken from the split working-half sections when necessary, and analysed to refine the ages between core catcher samples. Biostratigraphic analyses marked the first and last occurrences of key marker species of calcareous nanofossils, planktonic foraminifera and diatoms. Benthic foraminifera and ostracods were also used when applicable for age estimate determinations.

Shipboard palaeomagnetic investigations were conducted on both the archive and working halves of cores recovered during expeditions 367 and 368. The primary objectives were to determine the directions of natural remanent magnetization (NRM) components, including magnetic polarity, and downhole variation of magnetic properties. Shipboard measurements combined three complementary approaches: measurement and in-line alternating field (AF) demagnetization of archive-half sections on the pass-through 2G Enterprises (model 760R-4K) superconducting rock magnetometer (SRM), measurement and thermal demagnetization of oriented discrete samples on the SRM, and measurement and AF demagnetization of oriented discrete samples on the spinner magnetometer (AGICO model JR6). The palaeomagnetic age model was derived from the depth and timing of magnetic reversal events. The palaeomagnetic and palaeontological age constraints match well over most of the sections.

Seismic data and their correlation to drill cores. All seismic data shown were acquired at industry level quality by a commercial vendor. Multichannel seismic streamers (6,000 m length) were towed at 6–10 m depth with a shooting pattern resulting in a common depth point (CDP) distance of 6.25 m. Processing was done commercially to the highest industry standards and included deconvolution, multiple suppression, time migration and filtering. Several approaches were applied to correlate seismic data to the drill cores: wireline logging, continuous and discrete measurements of physical properties on the cores, vertical seismic profiling, check shots within the borehole, and ties between outstanding reflectors such as basement and regional distinct unconformities. The established core to seismic correlation was tested by synthetic seismogram modelling using wireline logging data and discrete physical properties data from the cores. Wireline logging data include natural gamma ray radiation, density, resistivity, acoustic velocity, magnetic susceptibility, formation microscanner, vertical seismic profiling (zero offset) and in situ temperature measurements and heat flow calculations. Physical properties measurements include bulk density, *p*-wave velocity, magnetic susceptibility, natural gamma rays, thermal conductivity and colour reflectance spectrometry.

Location of cited boreholes. Site U1499 (lat. N/long. E): 18° 24.57015′/115° 51.5955′. Site U1500: 18° 18.27345′/116° 13.19335′. Site U1501: 18° 53.0923′/115° 45.9455′. Site U1502: 18° 27.8759′/116° 13.8395′. Site U1435: 18° 33.3466′/116° 36.6174′.

Data availability. The data that support the findings of this study are available from the IODP Proceedings of Expeditions 367/368 (http://iodp.tamu.edu/publications/bibliographic_information/367368cit.html) to be published 28 September 2018. All IODP data from any expeditions can be obtained from https://doi.org/10.14379/iodp.proc.367368.2018. Further questions can be directed to the corresponding authors.

References

58. Sun, Z. et al. Methods. In *Proc IODP* (eds Sun, Z. et al.) Vol. 367/368, Ch. 2 (IODP, 2018); https://doi.org/10.14379/iodp.proc.367368.102.2018